The Astrophysical Journal, 919:6 (15pp), 2021 September 20 https://doi.org/10.3847/1538-4357/ac0cf8

A Massive Quiescent Galaxy Confirmed in a Protocluster at $z = 3.09$

Mariko Kubo[1,2], Hideki Umehata[3,4], Yuichi Matsuda[2,5], Masaru Kajisawa[1], Charles C. Steidel[6], Toru Yamada[7], Ichi Tanaka[8], Bunyo Hatsukade[4], Yoichi Tamura[9], Kouichiro Nakanishi[2,5], Kotaro Kohno[4,10], Kianhong Lee[4], and Keiichi Matsuda[9]

[1] Ehime University, 2-5 Bunkyo-cho, Matsuyama, Ehime, Japan; kubo@cosmos.phys.sci.ehime-u.ac.jp
[2] National Astronomical Observatory of Japan, 2-21-1 Osawa, Mitaka, Tokyo 181-8588, Japan
[3] RIKEN Cluster for Pioneering Research, 2-1 Hirosawa, Wako-shi, Saitama 351-0198, Japan
[4] Institute of Astronomy, Graduate School of Science, The University of Tokyo, 2-21-1 Osawa, Mitaka, Tokyo 181-0015, Japan
[5] Department of Astronomy, School of Science, The Graduate University for Advanced Studies, SOKENDAI, Mitaka, Tokyo 181-8588, Japan
[6] Cahill Center for Astronomy and Astrophysics, California Institute of Technology, MC 249-17, Pasadena, CA 91125, USA
[7] Institute of Space an Aeronautical Science, Japanese Aerospace Exploration Agency, 3-1-1, Yoshinodai, Chuo-ku, Sagamihara, Kanagawa, 252-5210, Japan
[8] Subaru Telescope, National Astronomical Observatory of Japan, 650 North A'ohoku Place, Hilo, Hawaii, 96720, USA
[9] Department of Physics, Nagoya University, Furo-cho, Chikusa-ku, Nagoya, Aichi 464-8601, Japan
[10] Research Center for the Early Universe, Graduate School of Science, The University of Tokyo, 7-3-1 Hongo, Bunkyo-ku, Tokyo 113-0033, Japan
Received 2021 January 9; revised 2021 June 17; accepted 2021 June 18; published 2021 September 16

Abstract

We report a massive quiescent galaxy at $z_{\rm spec} = 3.0922^{+0.008}_{-0.004}$ spectroscopically confirmed at a protocluster in the SSA22 field by detecting the Balmer and Ca II absorption features with the multi-object spectrometer for infrared exploration on the Keck I telescope. This is the most distant quiescent galaxy confirmed in a protocluster to date. We fit the optical to mid-infrared photometry and spectrum simultaneously with spectral energy distribution (SED) models of parametric and nonparametric star formation histories (SFHs). Both models fit the observed SED well and confirm that this object is a massive quiescent galaxy with a stellar mass of $\log(M_\star/M_\odot) = 11.26^{+0.03}_{-0.04}$ and $11.54^{+0.03}_{-0.00}$, and a star formation rate of SFR$/M_\odot\,{\rm yr}^{-1} < 0.3$ and $=0.01^{+0.03}_{-0.01}$ for parametric and nonparametric models, respectively. The SFH from the former modeling is described as an instantaneous starburst whereas that of the latter modeling is longer-lived, but both models agree with a sudden quenching of the star formation at ∼0.6 Gyr ago. This massive quiescent galaxy is confirmed in an extremely dense group of galaxies predicted as a progenitor of a brightest cluster galaxy formed via multiple mergers in cosmological numerical simulations. We discover three new plausible [O III]λ5007 emitters at $3.0791 \leqslant z_{\rm spec} \leqslant 3.0833$ serendipitously detected around the target. Two of them just between the target and its nearest massive galaxy are possible evidence of their interactions. They suggest the future great size and stellar mass evolution of this massive quiescent galaxy via mergers.

Unified Astronomy Thesaurus concepts: Galaxy evolution (594); Galaxy environments (2029); Giant elliptical galaxies (651); Protoclusters (1297)

1. Introduction

Deep multiwavelength imaging surveys have uncovered wide variations in galaxy populations at high redshift. Recently, massive quiescent galaxies at up to $z \sim 4$ have been discovered and confirmed spectroscopically (e.g., Daddi et al. 2005; van Dokkum et al. 2008; Kriek et al. 2009; Schreiber et al. 2018a; Tanaka et al. 2019; Forrest et al. 2020; Valentino et al. 2020). They are plausible progenitors of giant ellipticals today, though their formation mechanism is a challenging problem because they have to form a stellar mass $M_\star \gtrsim 10^{11}\,M_\odot$ and quench star formation in the early universe. Massive quiescent galaxies at high redshift are remarkably compact (a few to ten times smaller than local giant ellipticals) in general (e.g., Daddi et al. 2005; van Dokkum et al. 2008; Kriek et al. 2009; van der Wel et al. 2014; Kubo et al. 2018; Lustig et al. 2021). The centrally concentrated intense starburst triggered by e.g., gas rich major merger and/or violent disk instability is required to form such an object (e.g., Dekel et al. 2009; Burkert et al. 2010; Dekel & Burkert 2014; Zolotov et al. 2015). Recently, submillimeter galaxies (SMGs) with sizes, masses, and velocity dispersions similar to those of compact massive quiescent galaxies have been discovered and support this picture (e.g., Toft et al. 2014; Spilker et al. 2016; Valentino et al. 2020). It should also be considered that galaxies assembled in the early universe or when the universe was much denser tend to be compact (e.g., Williams et al. 2014; Wellons et al. 2015, 2016; Akhshik et al. 2021). Such massive quiescent galaxies at high redshift need strong size evolutions; scenarios involving evolutions of mass and size via mergers (e.g., Bezanson et al. 2009; Naab et al. 2009), expansion due to mass loss driven by feedback (e.g., Fan et al. 2008, 2010), and/or evolution of stellar population (van Dokkum et al. 2014) have been proposed but have not yet been constrained exactly.

Given the environmental dependence of galaxies today, we need to investigate the formation and evolution scenarios together with environments. However, massive quiescent galaxies at $z > 2$ in previous studies are mostly found in general fields or their environments are poorly explored, though several studies have reported possible overdensities around them (Strazzullo et al. 2015; Belli et al. 2017; Schreiber et al. 2018b, 2021). To properly track the formation history of giant ellipticals in clusters of galaxies in general, we also need to study their progenitors in protoclusters. The appearances of red sequences in protoclusters at $z \lesssim 3$ have been found by deep near-infrared (NIR) observations

(e.g., Kodama et al. 2007; Zirm et al. 2008; Doherty et al. 2010; Kubo et al. 2013; Strazzullo et al. 2016; Shi et al. 2020), and massive quiescent galaxies have been confirmed spectroscopically by detecting Balmer absorption features in clusters at up to $z \approx 2$ (Gobat et al. 2013). The environmental differences of the galaxy population at $z \sim 4$ have been shown statistically by using the deep and wide optical survey of the Hyper Suprime-Cam Subaru Strategic Program survey (Toshikawa et al. 2018; Kubo et al. 2019; Ito et al. 2020). However, morphologies of only a small number of massive quiescent galaxies have been studied (see Zirm et al. 2008 and Kubo et al. 2017, and also Strazzullo et al. 2013 and Mei et al. 2015 including mature clusters at $z \sim 2$), and the detailed spectral characteristics of massive quiescent galaxies have not yet been characterized in protoclusters.

We have studied a protocluster at $z = 3.09$ in the SSA22 field (Steidel et al. 1998), which is known as one of the most significant structures at high redshift. This structure was first identified by the overdensity of optically selected galaxies (Steidel et al. 1998; Hayashino et al. 2004; Matsuda et al. 2005; Yamada et al. 2012) and in later studies, was further characterized with the overdensity of active galactic nuclei (AGNs) selected in X-ray (Lehmer et al. 2009a, 2009b), SMGs (Tamura et al. 2009; Umehata et al. 2014, 2015, 2017, 2018), and dusty starburst and passively evolving galaxies selected photometrically based on the deep NIR imaging (Kubo et al. 2013). Thus, this protocluster is an ideal laboratory used to witness the transition of starburst galaxies into quiescent galaxies. In particular, the $2' \times 3'$ region containing the brightest SMG of this field was deeply observed with the Atacama large millimeter/submillimeter array (ALMA) and a significant overdensity of SMGs was discovered (Umehata et al. 2015, 2017, 2018; hereafter ADF22). They are clustering along the large-scale ($\sim$1 Mpc) Lyα filament, which indicates the supply of cold gas through a cosmic web (Umehata et al. 2019). The spatial and redshift distribution of galaxies (Matsuda et al. 2005; Kubo et al. 2015) suggest that this field is the central region of the SSA22 protocluster.

In this paper, we report the confirmation of a massive quiescent galaxy at the ADF22 field of the SSA22 protocluster by detecting the absorption features spectroscopically with the multi-object spectrometer for infrared exploration (MOSFIRE; McLean et al. 2012) on the Keck I telescope. This paper is organized as follows: In Section 2, we describe the target and observation with MOSFIRE and data analysis. In Section 3, we present the spectral energy distribution (SED) fittings and discoveries of new [O III] λ5007 emitters around this massive quiescent galaxy. In Section 4, we discuss the star formation history and future evolution scenario. We conclude in Section 5. In this study, we adopt cosmological parameters $\Omega_m = 0.3$, $\Omega_\Lambda = 0.7$ and $H_0 = 70$ km s^{-1} Mpc^{-1}. We assume the Chabrier (2003) Initial Mass Function (IMF). Magnitudes are expressed in the AB system.

2. Data and Analysis

2.1. Target

Previously, we conducted deep and wide NIR imaging observations of the SSA22 protocluster with the multi-object infrared camera and spectrograph (MOIRCS; Ichikawa et al. 2006; Suzuki et al. 2008) on the Subaru telescope over a field of $\approx$112 arcmin^2 for $K_s \approx 24$ at 5σ level, and found an overdensity of massive galaxies based on the photometric redshifts (z_{phot}) estimated with the SED fitting of the optical to MIR photometry (Kubo et al. 2013). Furthermore, we spectroscopically confirmed many of these candidates as protocluster members (Kubo et al. 2015). Among them, we selected candidate passively evolving galaxies based on the $i - K$ versus $K - [4.5]$ color following Labbé et al. (2005). These colors are similar to rest-frame UVJ often used to select quiescent galaxies (e.g., Whitaker et al. 2013). We selected galaxies satisfying $i - K > 3$ and $K - [4.5] < 0.5$, and $2.6 < z_{phot} < 3.6$ as candidate quiescent galaxies. The color criterion in Kubo et al. (2013) was set to avoid the contamination of dusty starburst galaxies detected in 24 μm that distribute at the border of the general color criteria for quiescent galaxies.

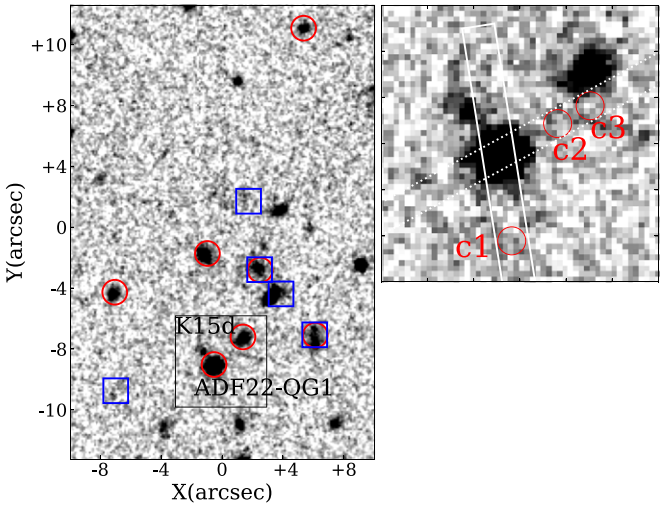

Figure 1. Left: The MOIRCS K_s-band image of the target field ($20''.0 \times 30''.0$). This is the newly obtained image described in Section 2.3. The red circles and blue squares show the objects spectroscopically confirmed at $3.0774 \leqslant z_{spec} \leqslant 3.0926$ with [O III] or Lyα (summarized in Kubo et al. 2016), and with CO(3–2) (Umehata et al. 2019) emission lines, respectively. Right: The zoomed-in image of the black square region in the left panel, which includes ADF22-QG1 and the adjacent massive galaxy, K15d ($6''.0$ by side). The white dashed and solid rectangles show the slit positions of the K-17 and $K(H)$-20 runs, respectively. The red circles ($0''.6$ diameter) show the positions of plausible [O III]λ5007 emitters detected simultaneously with ADF22-QG1 (Section 3.3).

Our target (R.A., decl. = 22:17:37.25, +00:18:16.0, hereafter ADF22-QG1) satisfies these selection criteria. It has a total magnitude of $K_{s,tot} = 21.55$. The SED is well-fitted with that of a single burst star formation history (SFH) model with an age of $\sim$1 Gyr at $z \sim 3.1$. We show the target on a rest-frame UVJ color diagram in Figure A1. Its spectroscopic redshift is limited to $z_{spec} = 2.7$ or 3.0–3.15 by detecting the 4000 Å break (Kubo et al. 2015). We took a high-resolution K'-band image of the target by using the adaptive optics AO188 and infrared camera and spectrograph (IRCS) on the Subaru telescope, and found that its effective radius (r_{eff}) is 1.01 ± 0.04 kpc (Kubo et al. 2017). Uniquely, it is likely in an extremely dense group of massive galaxies and SMGs identified by follow-up NIR spectroscopic observations of a 1.1 mm source found with ASTE/AzTEC (Kubo et al. 2016; hereafter AzTEC14 group). The left panel of Figure 1 shows the MOIRCS K_s-band image (described in Section 2.3) for $20'' \times 30''$ around the target. Apart from our target, there are nine galaxies at $3.0774 \leqslant z_{spec} \leqslant 3.0926$ confirmed by detecting the [O III] λ5007 and/or CO(3–2) emission lines (Kubo et al. 2016; Umehata et al. 2018). Assuming that they are hosted by the same halo, its expected halo mass is $\gtrsim 10^{13} M_\odot$ based on the velocity distribution (Kubo et al. 2016).

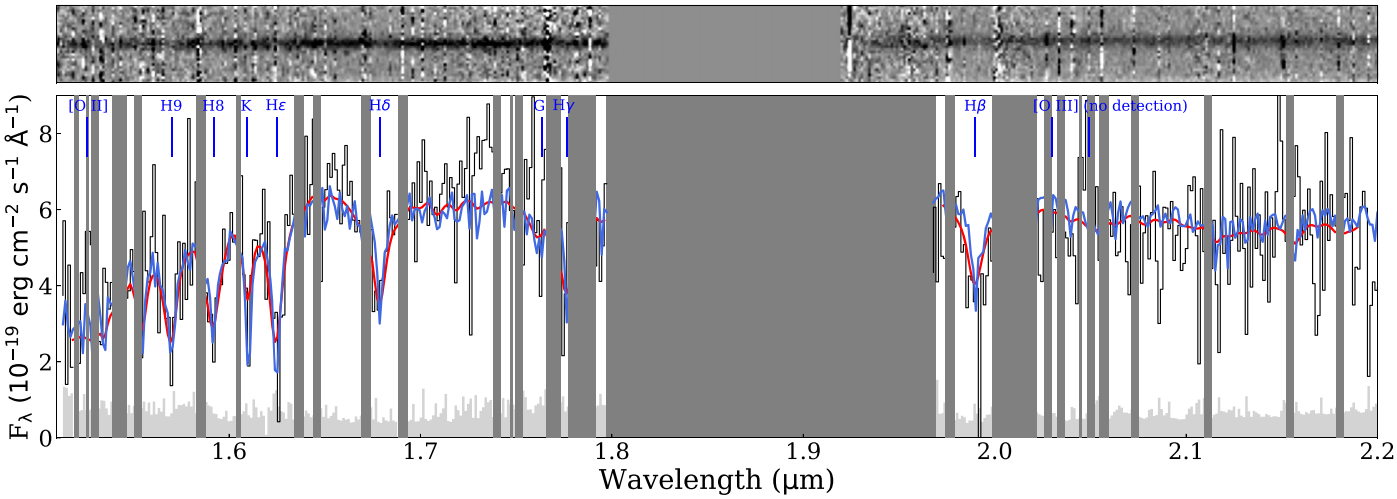

Figure 2. Top: The spectrum of ADF22-QG1 in the *H* and *K* bands, rebinned with ≈13 Å (6 pixels). Bottom: The black step plot shows the one-dimensional spectrum. The light gray filled histogram shows the 1σ noise at each bin. The red and blue curves show the best-fit SEDs obtained with FAST++ and continuity SFH prior of Prospector, respectively. The locations of the notable absorption features and of the [O II] and [O III] (no detection) emission lines are labeled.

2.2. Observation with MOSFIRE

We observed the target with MOSFIRE in *K* band in 2017 and 2020 September, and in *H* band in 2020 September (Hereafter *K*-17, *H*-20 and *K*-20). The right panel of Figure 1 shows the slit positions. The observations and data reduction are described in Umehata et al. (2019) (*K*-17) and in H. Umehata et al. (in prep) (*H*-20 and *K*-20). Briefly, the seeing conditions were 0.″7 ∼ 0.″9, 0.″6, and 0.″6 for the *K*-17, *K*-20, and *H*-20 runs, respectively. We adopted the two-position mask-nod sequence with 1.″5 dithers along slits with 120 (180) sec for each exposure in the *H*(*K*) band. The total exposure times at ADF22-QG1 were 2.5 and 6.5 hr (3.2 hr for *K*-17 and 3.3 hr for *K*-20) in the *H* and *K* bands, respectively. The spectra were reduced with the publicly available MOSFIRE data reduction pipeline, MCSDRP (Steidel et al. 2014).

We extracted the one-dimensional spectrum as follows to measure the fluxes of the spectrum and photometry consistently. Here, we calibrated the spectra to the *H*- and K_s-band photometry taken with MOIRCS (Section 2.4). First, the *H*-band spectrum was rebinned to match its pixel scale to that of the *K*-band spectrum (≈0″.18 pix^{-1} and 2.17 Å pix^{-1}) by using the magnify task of IRAF. Next, we combined the target and error spectra for ≈2.″0 in the spatial direction by an inverse variance weighting. Then, we measured the *H*- and K_s-band fluxes of the spectra by applying the transmission curve of the MOIRCS *H*- and K_s-band filters. Finally, we corrected the spectra to match these fluxes with the photometric fluxes.

2.3. Deeper K_s-band Image Taken with MOIRCS

We newly obtained a deeper K_s-band image with MOIRCS, which was upgraded in 2015 (nuMOIRCS; Fabricius et al. 2016; Walawender et al. 2016), on the Subaru telescope in July 2020 (PI: H. Umehata). We collected the images with PSF FWHM of 0.″3–0.″6 for 6.6 hr total exposure time. The data were reduced with the MOIRCS data reduction pipeline MCSRED.[11] We reduced the data using a standard procedure, but the flux is calibrated to our previous K_s-band image taken with MOIRCS (Kubo et al. 2013), which is calibrated to the UKIRT Infrared Deep Sky Survey (UKIDSS). The zero-point error is ≈0.05 mag relative to UKIDSS. Briefly, the final combined image has a PSF FWHM of 0.″40 and a 5σ limiting magnitude at a 0.″80 diameter of 25.34 mag.

2.4. Spectroscopic Redshift

Figure 2 shows the spectrum of ADF22-QG1. There are clear Balmer and Ca II absorption features, as well as an [O II]λ3727 emission line, while [O III]$\lambda\lambda$4959, 5007 emission lines are not detected significantly. Following Schreiber et al. (2018a), the spectroscopic redshift is estimated with SLINEFIT,[12] which fits a spectrum with combinations of a stellar continuum template and emission/absorption lines to find a redshift and line properties by a χ^2 minimization procedure. It returns a spectroscopic redshift $z_{\rm spec} = 3.0922^{+0.0008}_{-0.0004}$, which is consistent with the absorption features. Thus, ADF22-QG1 is certainly in the SSA22 protocluster, and moreover is a member of the dense group of galaxies discussed in Section 4.2. This is the most distant quiescent galaxy detected with Balmer absorption features in a protocluster. Hereafter, we adopt this spectroscopic redshift for ADF22-QG1.

The [O II] flux of ADF22-QG1 is $F_{\rm [O\,II]} = 5.7 \pm 1.0 \times 10^{-18}$ erg s^{-1} cm^{-2}. The SFR from [O II] luminosity is calculated as follows: First, the SFR from Hβ luminosity is computed assuming the case B recombination value intrinsic Hα/Hβ = 2.86 (Osterbrock & Ferland 2006), and the SFR to Hα luminosity relation in Kennicutt & Evans (2012),

$$\log {\rm SFR_{H\alpha}}(M_\odot\ {\rm yr^{-1}}) = \log {\rm L(H\alpha)(erg\ s^{-1})} - 41.27.$$

The normal star-forming galaxies (SFGs) at $z \sim 3$ have log [OII]/Hβ = 0.0–0.6 at most, according to Onodera et al. (2016). Then the SFR from [OII] is computed as

$${\rm SFR_{[O\,II]}}(M_\odot\ {\rm yr^{-1}}) = 4 - 15 \times 10^{-42}\ L_{\rm [O\,II]}({\rm erg\ s^{-1}}).$$

The $\rm SFR_{[O\,II]}$ for ADF22-QG1 is 2–7 $M_\odot$ yr^{-1} for $A_V = 0$ and 4–14 $M_\odot$ yr^{-1} for $A_V = 0.5$; these values are more than ten times higher than those from the SED fitting that we will describe later. [O II] emission lines are frequently seen in quiescent galaxies at high redshift, and the SFRs from [O II]

[11] https://www.naoj.org/staff/ichi/MCSRED/mcsred_e.html

[12] https://github.com/cschreib/slinefit

tend to be higher than those from SED modeling (e.g., Yan et al. 2006; Lemaux et al. 2010; Belli et al. 2015; Schreiber et al. 2018a). The [O II] flux of ADF22-QG1 is similar to those in previous studies. Taking the 2σ upper limit for [O III] ($\approx 2.3 \times 10^{-18}$ erg s^{-1} cm^{-2}), the [O III]/[O II] ratio of ADF22-QG1 is $\lesssim$0.4, corresponding to a H II region or LINER (Kewley et al. 2006). Since the [O III] flux upper limit corresponds to $\lesssim 2.4 \times 10^{42}$ erg s^{-1}, adopting the empirical [O III] to X-ray luminosity relation for type 2 AGN in Lamastra et al. (2009), it is no wonder that ADF22-QG1 is not detected with the Chandra observation of the SSA22 protocluster with a sensitivity limit $L_{2-10\,\mathrm{keV}} \approx 5.7 \times 10^{42}$ erg s^{-1} in Lehmer et al. (2009b). Based on the above, the [O II] emission of ADF22-QG1 may originate in a partly remaining star formation or weak AGN. Empirically, the excess [O II] of massive quiescent galaxies at high redshift is likely due to AGNs or LINERs rather than star formations (e.g., Yan et al. 2006; Lemaux et al. 2010).

2.5. SED Fitting

The absorption features together with multiwavelength photometry are strong constraints on the SFHs of massive quenched galaxies, as demonstrated in previous studies (e.g., Schreiber et al. 2018a; Belli et al. 2019; Forrest et al. 2020; Valentino et al. 2020; Akhshik et al. 2021; Tacchella et al. 2021). Here, we fit the spectrum and photometry of ADF22-QG1 simultaneously with the SED models with parametric SFHs by using FAST++,[13] and those of nonparametric SFHs by using Prospector[14] (Johnson & Leja 2017; Leja et al. 2017).

2.5.1. Data

First, we prepare the input photometric and spectroscopic data for SED modelings. We use the $u^{\star}BVRi'z'JHK_s$, 3.6, 4.5, 5.8, and 8.0 μm-band photometry measured in Kubo et al. (2013). Briefly, we convolve the $u^{\star}$ to K_s-band images to match the PSF to an FWHM of $\approx 1\farcs0$, and measure fluxes with a $2\farcs0$ diameter aperture. To match these, aperture correction is applied to the IRAC 3.6–8.0 μm photometry. The aperture correction factors are estimated using the K_s-band image (see details in Kubo et al. 2013). We also use the flux measured on the archival $F814W$-band image taken with the Advanced Camera and Spectrograph on Hubble Space Telescope (PID9760), using the same method, as well as an IR luminosity (at 8–1000 μm; L_{IR}) limit based on the 1.2 mm (256.98 GHz) image taken with ALMA in Cycle 2 (Umehata et al. 2018) and Cycle 5 (PID. 2017.1.01332.S, PI. H. Umehata, H. Umehata et al. 2021, in preparation). The L_{IR} is calculated by assuming the average 1.2 mm flux to L_{IR} relation for the SED library in Danielson et al. (2017). ADF22-QG1 is not detected at 1.2 mm, and the 3σ limiting flux is 75 μJy, corresponding to $L_{\mathrm{IR}} \sim 0.9$–$2.0 \times 10^{11}\,L_{\odot}$, taking the 95% confidence interval. The input observational data for Prospector is the same as that for FAST++, but the former uses L_{IR} while the latter uses the 1.2 mm flux.

We correct the aperture photometry and one-dimensional spectrum by multiplying them by 1.21, which is the ratio of the total (Kron) flux measured on the original image and the aperture flux measured on the PSF matched image in the K_s band. We also correct the Galactic extinction $E(B-V) = 0.053$ found from the dust extinction finding tool at NASA/IPAC INFRARED SCIENCE ARCHIVE[15] based on Schlafly & Finkbeiner (2011). The one-dimensional spectrum is rebinned with six pixels ($\approx$13 Å) by taking the inverse variance weighting average. The [O II] flux estimated with SLINEFIT is subtracted from the H-band photometry. The [O II] and strong OH airglow on the spectrum are excluded from the SED fitting. We use the spectrum at 1.51–1.80 and 1.97–2.19 μm, avoiding the spectrum with low transmission due to the instrument and/or sky. Both transmissions are still good, but we avoid using the spectrum at >2.19 μm because the nonuniformity of the sky transmission significantly remains on the reduced spectrum.

2.5.2. FAST++

First, we fit the spectrum and photometry simultaneously with SED models by using FAST++ following Schreiber et al. (2018a). We fit the SED with the Bruzual & Charlot (2003) stellar population synthesis models adopting the Chabrier (2003) IMF, Calzetti (2001) dust attenuation law, and the solar metallicity ($Z = 0.02$). We fit the models with extinction value $A_V = 0$–6 mag with steps of 0.1 mag and log (age yr^{-1}) = 7–9.3 with steps of 0.05 dex. We test an exponentially declining SFH (SFR $\propto \exp(-t/\tau)$); a delayed exponentially declining SFH ($\propto t \times \exp(-t/\tau)$), where t is time from the formation; and the composite SFH in Schreiber et al. (2018a). This SFH is described as a combination of

$$\mathrm{SFR_{base}(t)} \propto \begin{cases} e^{(t_{\mathrm{burst}}-t)/\tau_{\mathrm{rise}}} & \text{for } t > t_{\mathrm{burst}} \\ e^{(t_{\mathrm{burst}}-t)/\tau_{\mathrm{decl}}} & \text{for } t \leqslant t_{\mathrm{burst}} \end{cases} \quad (1)$$

and

$$\mathrm{SFR(t)} = \mathrm{SFR_{base}(t)} \times \begin{cases} 1 & \text{for } t > t_{\mathrm{free}} \\ R_{\mathrm{SFR}} & \text{for } t \leqslant t_{\mathrm{free}} \end{cases}, \quad (2)$$

where t is the lookback time. We fit in ranges $t_{\mathrm{burst}} = [10\,\mathrm{Myr}, t_{\mathrm{obs}}]$ with (logarithmic) steps of 0.05 dex, $\tau_{\mathrm{rise}}, \tau_{\mathrm{decl.}} = [10\,\mathrm{Myr}, 3\,\mathrm{Gyr}]$ with steps of 0.1 dex, $t_{\mathrm{free}} = [10\,\mathrm{Myr}, 300\,\mathrm{Myr}]$ with steps of 0.5 dex, and $R_{\mathrm{SFR}} = [10^{-2}, 10^{5}]$ with steps of 0.2 dex. The velocity dispersion applied for the templates in each FAST++ run is fixed. Then we run FAST++ with a velocity dispersion between 100 and 800 km s^{-1} with steps of 20 km s^{-1}.

2.5.3. Prospector

A parametric SED modeling can fail to reproduce a true SFH if a galaxy has a more complex SFH, e.g., starburst, sudden quenching, and rejuvenation. Then we also fit the SED with nonparametric models, which can handle with complex SFH following Leja et al. (2017, 2019). The fitting is performed by using Prospector (Johnson & Leja 2017; Leja et al. 2017), which uses the Flexible Stellar Population Synthesis (FSPS) code (Conroy et al. 2009). As in the FAST++ SED modeling, the Chabrier (2003) IMF and the Calzetti (2001) dust attenuation law are adopted. The two-component Charlot & Fall (2000) dust attenuation model is adopted in Prospector, while the uniform screen model is adopted in FAST++.

[13] https://github.com/cschreib/fastpp
[14] https://github.com/bd-j/prospector
[15] https://irsa.ipac.caltech.edu/applications/DUST/

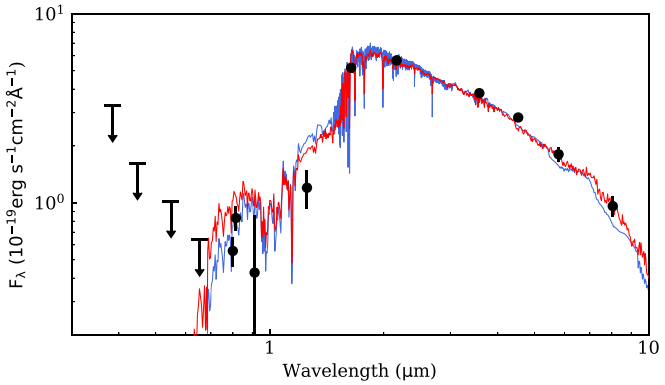

Figure 3. The black filled circles show the observed photometry of ADF22-QG1 with 1σ errors. The red and blue curves show the best-fit SEDs obtained with FAST++ and the continuity SFH prior of Prospector, respectively.

It consists of birth clouds and diffuse dust screen components. The dust attenuation is parameterized with the optical depths at 5500 Å of these two components, $\hat{\tau}_1$ (birth clouds) and $\hat{\tau}_2$ (diffuse dust). In the case of the Calzetti (2001) dust attenuation law, $\hat{\tau}_1$ is set to zero and the dust attenuation is controlled only with $\hat{\tau}_2$. We adopt the result measured adopting the solar metallicity ($Z = 0.02$).

We use a continuity SFH prior that fits directly for $\Delta\log$ (SFR) between adjacent time bins. Here, the adopted time bins are $0 < \log(\text{age yr}^{-1}) < 7.5$, $7.5 < \log(\text{age yr}^{-1}) < 8.0$, and $\Delta\log(\text{age yr}^{-1}) = 0.11$ binning at the range $8.0 < \log(\text{age yr}^{-1}) < 9.3$ (14 time bins in total). The free parameters are $\log(M_\star/M_\odot)$ (between 7 and 12), $\Delta\log$ (SFR) between adjacent time bins (scale = 0.3, df = 2), and $\hat{\tau}_2$ (between 0.0 to 2.0). The sampling is performed with the nested sampler dynesty (Speagle 2020), and the maximum *a posteriori* (MAP) values are presented as the best-fit quantities.

Though we adopt the above model, we also test the continuity SFH model with free metallicity, as well as the prospector-α (Leja et al. 2017) model. The latter model adopts a Dirichlet SFH prior, the prescription of a dust attenuation law from Noll et al. (2009) that allows a flexible dust attenuation law slope and $\hat{\tau}_1$ to $\hat{\tau}_2$ ratio, and adds an AGN contribution. We summarize the results of these different modelings in Appendix B. Briefly, the results do not depend on the dust attenuation law and the contribution of AGN is negligible. The model with near-solar metallicity is favored for the continuity-SFH model but low metallicity is favored for the Prospector-α (Dirichlet) model, though our data have no significant spectral indices to determine the metallicity definitely. A model with lower metallicity tends to have an SFH in which the star formation quenches earlier. Thus, we here adopt the continuity-SFH model with the solar metallicity ($Z = 0.02$) as the conservative model.

3. Result

3.1. SED: FAST++

The red curves in Figures 2 and 3 show the best-fit SED, and Table 1 lists the SED parameters and SFH quantities found with FAST++. We note that there is no significant difference between the SED quantities and SFHs derived with the three SFH models. Here, we adopt the best-fit model found with the composite SFH modeling to compare the results directly with literature (Schreiber et al. 2018a; Forrest et al. 2020; Valentino et al. 2020). The SFH and several SFH quantities, $\langle\text{SFR}\rangle_{\text{main}}$, t_{50} and t_q, are computed with FAST++. The $\langle\text{SFR}\rangle_{\text{main}}$ is the mean SFR during the shortest time interval over which 68% of the star formation took place. The formation time t_{50} is the time at which 50% of the total stellar mass has been formed, excluding mass loss and recycling, and the quenching time t_q is the elapsed time since the SFR dropped below 10% of the $\langle\text{SFR}\rangle_{\text{main}}$. Both t_{50} and t_q are given as a lookback time from the observed redshift. The uncertainties of the values from the SED modeling in Table 1 are the 90% confidence interval values.

Table 1
Physical Properties

Properties	ADF22-QG1
z_{spec}	$3.0922^{+0.0008}_{-0.0004}$
r_{eff}/kpc[a]	1.01 ± 0.04
$\log(M_{\star,\text{FAST++}}/M_\odot)$	$11.26^{+0.03}_{-0.04}$
$\log(M_{\star,\text{continuity}}/M_\odot)$	$11.54^{+0.03}_{-0.00}$
$\text{SFR}_{\text{FAST++}}/M_\odot\ \text{yr}^{-1}$	<0.3
$\text{SFR}_{\text{continuity}}/M_\odot\ \text{yr}^{-1}$	$0.01^{+0.03}_{-0.01}$
$\text{SFR}_{(\text{O II})}/M_\odot\ \text{yr}^{-1}$	2–14
$\text{SFR}_{\text{IR}}/M_\odot\ \text{yr}^{-1}$	$<$9–21
$\text{sSFR}_{\text{FAST++}}/\text{yr}^{-1}$	$<1.8 \times 10^{-12}$
$\text{sSFR}_{\text{continuity}}/\text{yr}^{-1}$	$0.7^{+10.3}_{-0.7} \times 10^{-14}$
$\text{sSFR}_{(\text{O II})}/\text{yr}^{-1}$[b]	$1–8 \times 10^{-11}$
$\text{sSFR}_{\text{IR}}/\text{yr}^{-1}$[b]	$<5–12 \times 10^{-11}$
$A_{V,\text{FAST++}}$/mag	$0.5^{+0.1}_{-0.1}$
$\hat{\tau}_{2,\text{continuity}}$	$0.13^{+0.02}_{-0.02}$
$\log(t_{50,\text{FAST++}}/\text{yr})$	$8.79^{+0.05}_{-0.05}$
$\log(t_{50,\text{continuity}}/\text{yr})$	$9.08^{+0.08}_{-0.02}$
$\log(\langle\text{SFR}\rangle_{\text{main,FAST++}}/M_\odot\ \text{yr}^{-1})$	$4.06^{+0.45}_{-1.23}$
$\log(\langle\text{SFR}\rangle_{\text{main,continuity}}/M_\odot\ \text{yr}^{-1})$	$2.31^{+0.06}_{-0.04}$
$\log(t_{q,\text{FAST++}}/\text{yr})$	$8.78^{+0.04}_{-0.20}$
$\log(t_{q,\text{continuity}}/\text{yr})$	8.80–8.91
$\log(\tau_{\text{decl.,FAST++}}/\text{yr})$	$7.0^{+2.5}_{-0.0}$

Notes.
[a] Kubo et al. (2017).
[b] Adopting $M_{\star,\text{FAST++}}$ as an upper limit value.

The best-fit model and its reduced χ^2 value change marginally if we set a different velocity dispersion. We also tried the penalized pixel-fitting algorithm (pPXF; Cappellari 2017) but could not also obtain a robust velocity dispersion estimate. This is because all the available Balmer absorption features are partly covered by OH airglow. Here, we show the best-fit parameters for velocity dispersion = 320 km s^{-1} where the χ^2 value minimizes ($\chi^2/\nu = 2.7$). We also test the models with metallicities 0.2, 0.4, and 2.5 $Z_\odot$, but this also do not change the results significantly. A corner plot for covariance among the age, A_V, Z, SFR, $M_\star$, t_{50}, and t_q is presented in Figure B2, which shows that the stellar population of ADF22-QG1 is well-constrained with small degeneracy.

ADF22-QG1 is well-fitted with an SED model suppressed star formation. Its specific SFR ($\text{sSFR}_{\text{FAST++}}$) $< 1.8 \times 10^{-12}\ \text{yr}^{-1}$. The L_{IR} limit for ADF22-QG1 corresponds to SFR $<$ 9–21 $M_\odot\ \text{yr}^{-1}$ using the L_{IR} to SFR conversion factor in Kennicutt & Evans (2012). Note that the L_{IR} and thus SFR_{IR} based on a single-band flux depend greatly on the adopted SED models (Santini et al. 2019; Mizukoshi et al. 2021). Scaling the 1.2 mm flux limit of our target to the model prediction in Santini et al. (2019), it can have an SFR_{IR} upper limit $\lesssim 100\,M_\odot\ \text{yr}^{-1}$. Even though we adopt

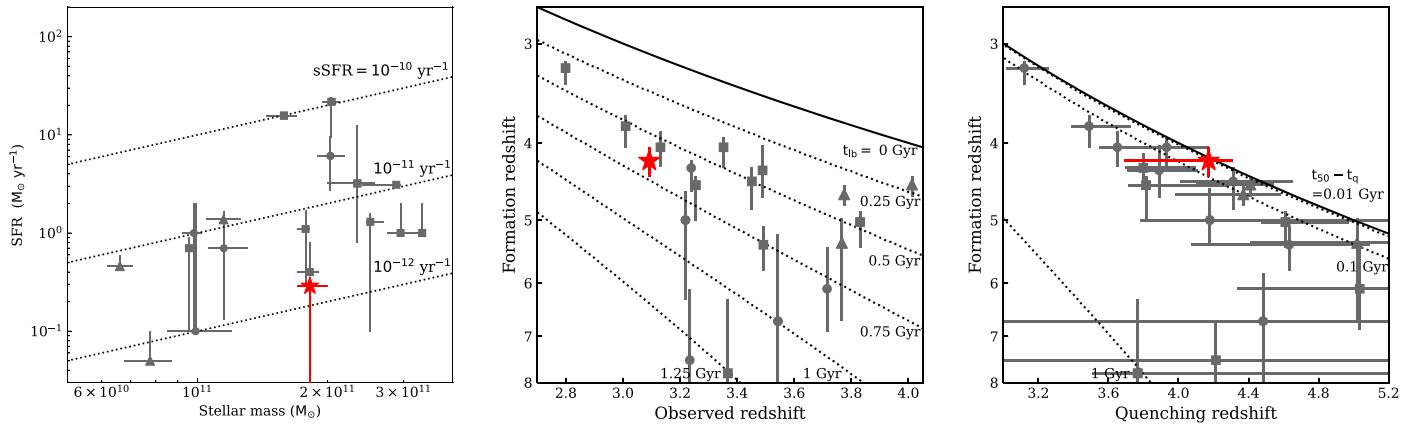

Figure 4. The comparison of the SED quantities. The red star shows ADF22-QG1. The gray circles, squares, and triangles show quenched galaxies in Schreiber et al. (2018a), Forrest et al. (2020), and Valentino et al. (2020). Left: The stellar mass vs. SFR. The dotted curves show the sSFR of 10^{-10} yr^{-1}, 10^{-11} yr^{-1}, and 10^{-12} yr^{-1}. Center: The observed redshifts vs. formation redshifts. The dotted curves show the lookback times from the observed redshifts with 0.25 Gyr steps. Right: The quenching redshifts vs. formation redshifts. The dotted curves show the time durations between formation and quenching redshifts of 0.01, 0.1, and 1 Gyr.

the $SFR_{[O\ II]}$ or SFR_{IR} at the upper limit, ADF22-QG1 is classified as a quenched galaxy. We put the SFH evaluated with FAST++ in Figure B1, where the whole stellar mass is formed instantaneously. The formation time t_{50} of ADF22-QG1 is younger ($0.62^{+0.09}_{-0.05}$ Gyr) than that estimated from the fitting only with the photometry ($\gtrsim$1 Gyr). This is expected from the spectral characteristic of ADF22-QG1 that the 4000 Å break is strong but Balmer absorption features are still significant. Such an SFH cannot be measured robustly without deep NIR spectroscopic observations like this study.

Figure 4 compares the SED quantities of ADF22-QG1 and those of quenched galaxies at $2.8 < z_{spec} < 4.0$ in the literature (Schreiber et al. 2018a; Forrest et al. 2020; Valentino et al. 2020). The star formation of ADF22-QG1 is suppressed well among them. ADF22-QG1 has formed later but more rapidly than other quiescent galaxies. At this point, we find no significant environmental dependence in the SED quantities. Note that the figure appears to be lacking slowly quenched ($t_{50} - t_q > 0.1$ Gyr) galaxies; however, this is likely the sample bias that quiescent galaxies at $z > 3$ quenched earlier than the current sample are hardly surveyed completely at the current survey depth $K_s \lesssim 24$ mag (Forrest et al. 2020).

3.2. SED: Nonparametric

The best-fit SED from nonparametric modeling of SFH is shown with blue curves in Figures 2 and 3. It also fits the observed SED well. The SED quantities from nonparametric modeling are subscripted with continuity in Table 1. Figure B3 shows a corner plot for covariance among the fitting parameters in the nonparametric modeling.

Both the nonparametric and parametric modeling fit the observed SED with a model of massive galaxy with suppressed star formation ($sSFR_{continuity} = 0.7^{+10.3}_{-0.7} \times 10^{-14}$ yr^{-1}). However, they find different SFHs and stellar masses. Figure 5 shows the SFH evaluated with nonparametric modeling. It is flatter than that from FAST++ and does not take an extreme value. The SFR drops sharply after the time bin $8.80 < \log(\text{age yr}^{-1}) < 8.91$ or the star formation is quenched during this time bin. It agrees very well with the quenching time $\log(t_{q,FAST++}/\text{yr}) = 8.78^{+0.04}_{-0.20}$ from FAST++. Because of the larger contribution from old stars, the stellar mass from nonparametric modeling is twice as large as that from FAST++.

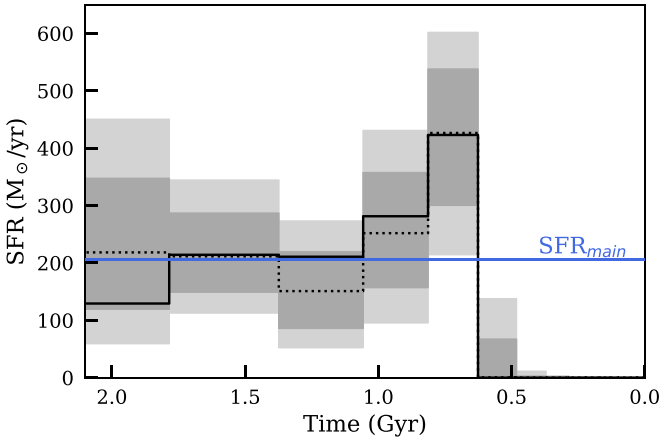

Figure 5. The SFH evaluated adopting the continuity SFH prior with Prospector. The black solid histogram shows the MAP value. The gray shaded region and dotted line show the 16th, 50th, and 84th percentiles of the posterior. The light gray shaded region show the 5th and 95th percentiles of the posterior.

3.3. Newly Detected [O III] Emitters

Adjacent to ADF22-QG1, emission lines are detected at three positions between 2.042 and 2.045 μm (Figure 6, hereafter c1, c2, and c3). We extract their one-dimensional spectra by combining the spectra for $\approx$1.″3 and 2.″2 in the spatial direction for c1, and c2 & c3, respectively, and smoothing them with three pixels in the wavelength direction. We fit the one-dimensional spectra with Gaussian profiles by a standard χ^2 minimization procedure. We derive them under the assumption that they are [O III]λ5007.

We estimate their sky positions based on the average spatial profiles in a range $\approx$17 Å (8 pixels) at emission lines (Figure 6, top right). In the case of c1 and c3, they show clear peaks at 1.″6 and 2.″3 from ADF22-QG1. The peak of c2 is not so clear, but likely falls between c3 and ADF22-QG1. Their K_s-band magnitudes measured with 0.″80 diameter apertures are $<$26.34 ($<2\sigma$), 26.02 (2.7σ), and 25.72 (3.5σ), respectively. Table 2 summarizes their observed properties. Interestingly, the spatial locations and redshifts of c2 and c3 are just between ADF22-QG1 and the nearest massive galaxy, K15d at $z_{spec} = 3.0774 \pm 0.0003$ (Kubo et al. 2016).

Table 2
Newly Detected [O III] Sources

ID	R.A. (J2000)	Decl. (J2000)	z_{spec}	$F_{(O\ III)}$ (10^{-18} erg cm^{-2})	K_s (mag)
c1	22:17:37.24	+0:18:14.2	3.0811 ± 0.0001	0.9 ± 0.2	<26.34[a]
c2	22:17:37.17	+0:18:16.7	3.0833 ± 0.0003	0.9 ± 0.2	26.02
c3	22:17:37.13	+0:18:17.1	3.0791 ± 0.0001	1.1 ± 0.2	25.72

Note.
[a] 2σ limiting flux.

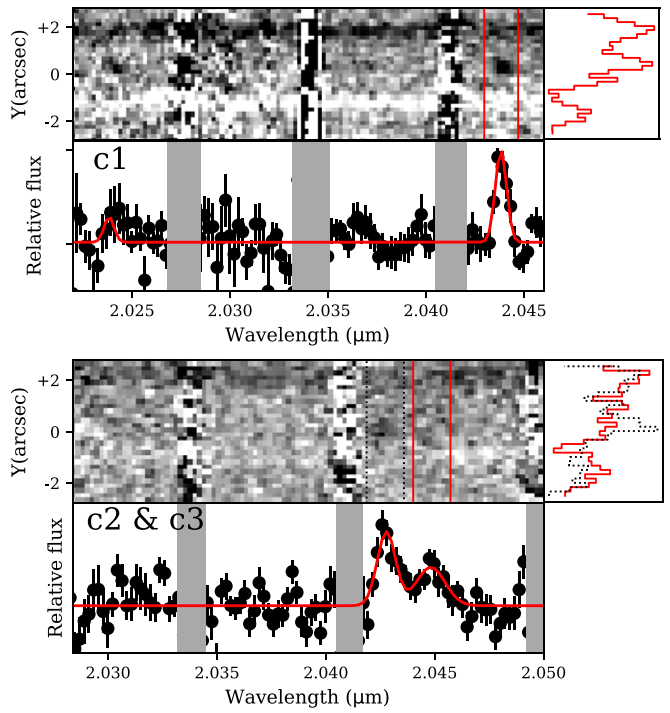

Figure 6. Top: The spectrum at c1. The left panel shows the spectrum image. The bottom panel shows the one-dimensional spectrum. Black points show the observed spectrum. The gray shaded regions show OH airglow masked when we fit the spectrum. The red curve shows the Gaussian fit of the spectrum. The top right shows the spatial profile of the spectrum measured between the red solid lines in the bottom panel. Bottom: Similar to the top panel, but for c2 (redder) and c3 (bluer). The spatial profiles of the spectra are shown at two wavelength ranges corresponding to c2 and c3 (red solid and black dashed lines).

4. Discussion

4.1. SFH

Both the parametric and nonparametric modeling of the SFH find that ADF22-QG1 is rapidly quenched at ∼0.6 Gyr ago. To reproduce such a sudden quenching, strong feedbacks are needed (e.g., Belli et al. 2019; Rodríguez Montero et al. 2019; Forrest et al. 2020). If the SFH of ADF22-QG1 is like that estimated with FAST++, feedback from young massive stars is applicable for the quenching (Murray et al. 2005). The quenching via AGN feedback cannot be ignored, especially for massive galaxies. ADF22-QG1 is not detected with Chandra, but its [O II] could originate in a dying AGN. We will further discuss the roles of AGNs for the evolution of protocluster galaxies in an upcoming paper. Another problem that is beyond the scope of this paper but ought to be solved in the future is the question of how ADF22-QG1 has maintained its quiescence for several 100 Myr although it is in a gas-rich environment and surrounded by starbursting neighbors (Umehata et al. 2019) that can induce further starburst.

Which SFH is more realistic? The $\langle SFR\rangle_{main,FAST++}$ of ADF22-QG1 is not so realistic because it is even higher than those of the brightest SMGs with SFR $\lesssim 5000\,M_\odot$ yr^{-1} (Riechers et al. 2013; Oteo et al. 2016; Spilker et al. 2020). Theoretically, if the SFR surface density of an SFG reaches the Eddington limit where momentum-driven wind is induced by radiation pressure on dust heated by young massive stars, its star formation can be suppressed (Murray et al. 2005). The limiting SFR surface density for SMGs is $\sim 1000\,M_\odot$ yr^{-1} kpc^{-2}, based on Andrews & Thompson (2011). SMGs do not exceed this limit in general (Simpson et al. 2015), while the brightest SMGs are near this limit. The SFR surface density of ADF22-QG1 at $\langle SFR\rangle_{main,FAST++}$ computed by dividing it with an area with a radius of the twice r_{eff} at the observed redshift is $0.86^{+1.67}_{-0.78} \times 10^3\ M_\odot\,yr^{-1}\,kpc^{-2}$, which by far exceeds the Eddington limit SFR surface density.

Thus, the SFH from nonparametric modeling is more realistic. The SFR of ADF22-QG1 before quenching is consistent with or lower than those of the observed SMGs in protoclusters at $z \sim 4$ (e.g., Miller et al. 2018; Oteo et al. 2018; Pavesi et al. 2018; Long et al. 2020) and the SSA22 protocluster itself (Umehata et al. 2018). Our argument could also be true for the other massive quiescent galaxies at $z > 3$ in literature in which parametric SED modelings are widely used. In these studies, the SFHs are often described as a vigorous starburst similar to ADF22-QG1 computed with FAST++ (e.g., Schreiber et al. 2018a; Forrest et al. 2020; Valentino et al. 2020). Then the most active starburst galaxies, like SMGs, have SFRs in concordance with the SFH for massive quiescent galaxies. However, to explain the observed properties, e.g., number densities, less-bursty SFGs on the star formation main sequence are also needed to be the major progenitors of massive quiescent galaxies (Barro et al. 2013, 2017; Popping et al. 2017; Gómez-Guijarro et al. 2019; Valentino et al. 2020). In addition, observed stellar masses of the brightest SMGs at $z > 3$ are often larger than those of massive quiescent galaxies at $3 < z < 4$ (Valentino et al. 2020). Adopting the SFH from nonparametric modeling, massive SMGs and main sequence SFGs are allowed as a progenitor of ADF22-QG1. Although we need a further robust SFH measurement in the future, application of SFHs more complex than typical parametric SFHs can correct the relation between massive quiescent galaxies and high-z SFGs.

4.2. Size and Mass Evolution

Here, we confirm a compact massive quiescent galaxy as a secure progenitor of a giant elliptical or brightest cluster galaxy (BCG) in a cluster of galaxies today. Similarly, it has been reported that massive quiescent galaxies in protoclusters/clusters

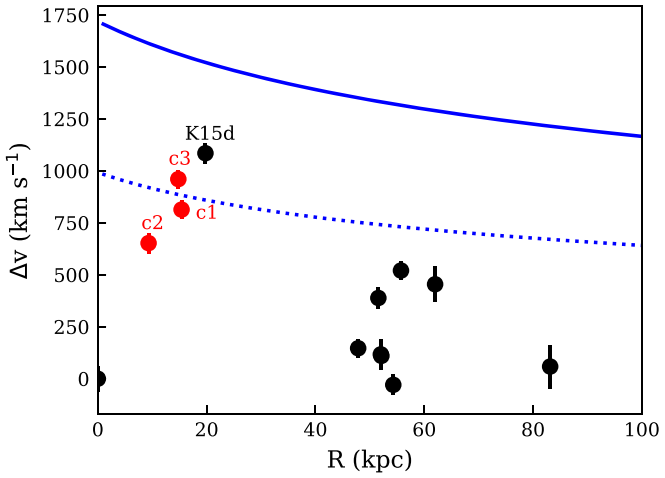

Figure 7. The line-of-sight velocities and spatial distances of the galaxies relative to the ADF22-QG1. The black points are based on the redshifts of galaxies listed in Kubo et al. (2016) and Umehata et al. (2019), while the red points show the [O III] emitters confirmed in this study. The blue solid curve shows the escape velocity for an NFW halo with a halo mass $1.1 \times 10^{13}\,M_{\odot}$ (virial radius = 170 kpc and concentration $c = 5$). The blue dashed curve shows the projected escape velocity (the velocity and distance are divided with $\sqrt{3}$ and $\sqrt{3/2}$, respectively).

at $z \lesssim 2$ are more compact than nearby giant ellipticals in Zirm et al. (2008), Strazzullo et al. (2013), and Mei et al. (2015). It needs a strong size evolution to evolve into a typical giant elliptical or BCG. Cosmological numerical simulations predict that a BCG is hierarchically formed via multiple mergers of galaxies (e.g., De Lucia & Blaizot 2007). Supporting such a scenario, ADF22-QG1 is not isolated; it lies in a dense group of massive galaxies and SMGs. Figure 7 shows the velocity distribution of galaxies within 100 physical kpc from ADF22-QG1. We use the redshifts derived from [O III] and/or CO(3–2) lines in Kubo et al. (2016) and Umehata et al. (2019) (black), as well as the newly confirmed [O III] emitters (red) discussed in this study. The redshift of ADF22-QG1 is certainly close to the group members, though it is offset from the median redshift $z_{\rm med} = 3.087$ of the group. Their velocity dispersion is $\sigma_v = 351 \pm 52$ km s^{-1}, as evaluated by a bootstrap resampling. According to the scaling relation based on *N*-body simulations in Evrard et al. (2008),

$$\sigma_{\rm DM}(M, z) = \sigma_{\rm DM,15}\left[\frac{h(z)M_{200}}{10^{15}M_{\odot}}\right]^{\alpha},$$

where $h(z) = H(z)/100$ km s^{-1} and $\sigma_{\rm DM,15}$ is the normalization for a halo mass $10^{15}\,{\rm h}^{-1}\,M_{\odot}$. They found $\sigma_{\rm DM,15} = 1082.9 \pm 4.0$ km s^{-1} and $\alpha = 0.3361 \pm 0.0026$ for ΛCDM cosmology. Adopting the above σ_v, the halo mass of AzTEC14 group is $1.1 \pm 0.4 \times 10^{13}\,M_{\odot}$, consistent with our previous measurement (Kubo et al. 2016). The velocity offsets of all the group members are below the escape velocity for a halo characterized with the above halo mass and NFW (Navarro et al. 1997) profile.

The velocity distribution and halo mass of the AzTEC14 group are similar to those of SPT234956, which is known as an extreme overdensity of SMGs at $z = 4.3$ (Miller et al. 2018; Hill et al. 2020). Rotermund et al. (2021) shows that the stellar mass of the most massive member and total stellar mass of SPT234956 are at least $3.2^{+2.3}_{-1.4} \times 10^{11}\,M_{\odot}$ and $(12.2 \pm 2.8) \times 10^{11}\,M_{\odot}$, respectively. Correcting the total stellar mass of the $K_{\rm s}$-band detected galaxies of the AzTEC14 group found in Kubo et al. (2016) with the newly measured stellar mass for ADF22-The total stellar mass of QG1 from the nonparametric SFH modeling is at least $6.7^{+2.3}_{-0.8} \times 10^{11}\,M_{\odot}$, which is comparable to or lower than SPT234956. On the other hand, SPT234956 is far more luminous at submm than the SSA22 protocluster (Miller et al. 2018), i.e., the star formation in AzTEC14 group is less active. SPT234956 is a close analog of the AzTEC14 group, but a larger stellar mass will be assembled in the former.

Rennehan et al. (2020) simulated the assembly history of BCGs by performing isolated non-cosmological hydrodynamical simulations based on the observed properties of SPT234956. They predicted that all the group members at $z = 4.3$ merge into one massive galaxy by ∼0.5 Gyr. The spectroscopic confirmation of ADF22-QG1 in the AzTEC14 group and newly confirmed [O III] emitters, which are possible evidence of interactions between ADF22-QG1 and K15d, further support such an early BCG assembly scenario via multiple mergers. We discussed the size and stellar mass growths of ADF22-QG1 via mergers based on the observed sizes and stellar masses of the AzTEC14 group members in Kubo et al. (2017). Assuming no further stellar mass and size growth in each group member, and that all mergers are dry, the size and stellar mass of ADF22-QG1 can increase by 3–4 times and double via mergers of all the group members, respectively. If ADF22-QG1 is just a progenitor of a giant elliptical, this scenario is sufficient. However, to grow ADF22-QG1 into a BCG, further size and stellar mass growth in each group member and/or further mergers of external galaxies are required. This argument does not change greatly if we adopt the newly measured stellar mass for ADF22-QG1 in this study. Further consideration of the newly confirmed SMGs in Umehata et al. (2019), in particular their size and stellar mass growth, as well as stellar/AGN feedbacks in the AzTEC14 group, should be the foci of future studies. Finally, we note that ADF22-QG1 is not the only candidate progenitor of the BCG of the SSA22 protocluster, since there are several such extremely dense groups of galaxies (Kubo et al. 2016; Umehata et al. 2018).

5. Conclusion

We confirm a massive quiescent galaxy at the core of a protocluster at $z = 3.09$ in the SSA22 field. This is the most distant quiescent galaxy confirmed with Balmer absorption features in a protocluster to date, and a securely selected giant elliptical/BCG progenitor. We fit the observed SED with both parametric and nonparametric models of SFHs. Both models agree that our target is a massive galaxy with suppressed star formation. The SFH found with the parametric modeling is described as a short starburst, while that of the nonparametric modeling is a longer-lived SFH. The SFH found with the nonparametric modeling is more realistic, given the extremely high SFR surface density in the past derived from parametric modeling. On the other hand, both models support that the star formation was suddenly quenched after a starburst ∼0.6 Gyr ago. To reproduce this, a strong feedback is required. This massive quiescent galaxy is confirmed as a member of an extremely dense group of massive galaxies and SMGs predicted as a progenitor of a BCG in cosmological numerical simulations. According to the simulations, such a system will merge into one massive galaxy within ∼0.5 Gyr. We also newly confirm three plausible [O III] emitters around this

quiescent galaxy. Two of them are possible evidence of the interaction between the quiescent galaxy and its nearest massive galaxy. They strongly support a hierarchical formation scenario of BCGs.

It is still unclear what the major formation and quenching mechanisms are, as well as how to maintain the quiescence of our target for several 100 Myr in such a dense environment. Topics for future study include older and fainter quiescent galaxies, the roles of AGNs in protoclusters, and the stellar (gas and star formation) surface densities of galaxies, which may correlate with the SFH and quenching mechanism. Such studies, facilitated by the James Webb Space Telescope (JWST) and Nancy Grace Roman Space Telescope (NGRST), will enable us to discuss the typical formation scenario of cluster galaxies.

We thank the anonymous referee for a number of useful suggestions. This work is supported by JSPS KAKENHI grant Numbers 20K14530 (MK), 17K14252, 20H01953 (HU), 17KK0098 (YM), 19K0397 (KN), and 17H06130 (KK). The spectroscopic data were obtained at the W. M. Keck Observatory, which is operated as a scientific partnership among the California Institute of Technology, the University of California, and the National Aeronautics and Space Administration. The observations were carried out within the framework of Subaru-Keck/Subaru-Gemini time exchange program, which is operated by the National Astronomical Observatory of Japan. The K_s-band image was collected with nuMOIRCS at Subaru Telescope, which is operated by the National Astronomical Observatory of Japan. We are honored and grateful for the opportunity of observing the universe from Maunakea, which has cultural, historical, and natural significance in Hawaii. This paper makes use of the following ALMA data: ADS/JAO.ALMA#2013.1.00162.S, ADS/JAO.ALMA#2017.1.01332.S. ALMA is a partnership of ESO (representing its member states), NSF (USA), and NINS (Japan), together with NRC (Canada), MOST and ASIAA (Taiwan), and KASI (Republic of Korea), in cooperation with the Republic of Chile. The Joint ALMA Observatory is operated by ESO, AUI/NRAO and NAOJ. The *F*814*W*-band image is based on observations made with the NASA/ESA Hubble Space Telescope, obtained from the data archive at the Space Telescope Science Institute. STScI is operated by the Association of Universities for Research in Astronomy, Inc. under NASA contract NAS 5-26555.

Appendix A
UVJ Color Diagram

Figure A1 shows the rest-frame UVJ color diagram for ADF22-QG1. The red star shows the rest-frame UVJ colors of ADF22-QG1 estimated with the SED fitting. The points and curves show the color evolution tracks for SED models with ages between 0.1 to 2 Gyr as computed with GALAXEV (Bruzual & Charlot 2003). The black solid line shows the color criterion for quiescent galaxies at 2.0 $0.88 \times (V - J)+0.59$, $(U - V) > 1.2$, and $(V - J) < 1.4$ in Whitaker et al. (2013).

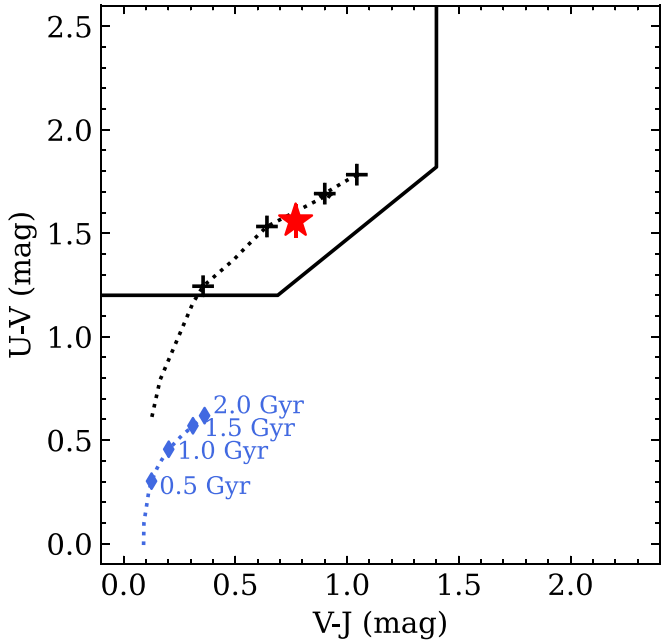

Figure A1. The rest-frame *UVJ* color diagram for ADF22-QG1. The red star shows the rest-frame *UVJ* colors of ADF22-QG1 estimated with the SED fitting. The points and curves show the color evolution tracks for SED models with ages between 0.1 to 2 Gyr as computed with GALAXEV (Bruzual & Charlot 2003). The black crosses with dotted curve show the color evolution track for a single burst star formation model with $A_V = 0$. The blue diamonds and curve show the color evolution track for a constant star formation model with $A_V = 0$. The points are shown at ages 0.5, 1.0, 1.5, and 2.0 Gyr. The black solid line shows the color criterion for quiescent galaxies at $2.0 < z < 3.5$ in Whitaker et al. (2013).

Appendix B
The Corner Plots and SFHs for Various Models

Here, we present the SFHs obtained with various models. First, we show the SFH and the corner plot for the main quantities evaluated with FAST++ in Figures B1 and B2, respectively. The corner plots presented in this paper are generated with corner.py (Foreman-Mackey 2016). In this model SFH, star formation occurs almost instantaneously. This model can explain the observed SED, but results in unrealistically high maximum SFR.

We also present the nonparametric SFHs evaluated with Prospector. Here, we show the SFHs evaluated adopting the models: i) Continuity SFH fixed with the solar metallicity (shown in Figure 5 in main text), (ii) Continuity SFH with free metallicity ($-2.0 \log Z/Z_\odot < 0.2$), (iii) Prospector-$\alpha$ SFH fixed with the solar metallicity, and (iv) Prospector-α SFH with free metallicity ($-2.0 \log Z/Z_\odot < 0.5$).

The continuity SFH adopted in (i) and (ii) models is described in Section 2.5.1. The Prospector-α model is the model adopted in Leja et al. (2017). This model uses the Dirichlet SFH prior, as well as the dust attenuation law prescription in Noll et al. (2009), and adds an AGN component. In this prior, the fractional sSFR in each time bin follows a Dirichlet distribution. The dust attenuation model in Prospector is the Charlot & Fall (2000) model consisting of birth

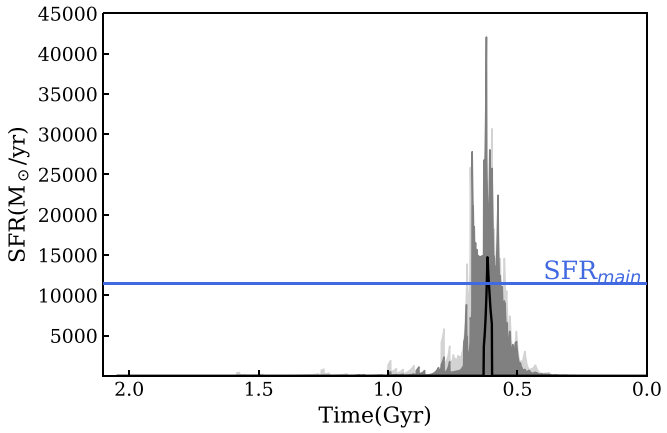

Figure B1. The SFH evaluated with FAST++. The black curve shows the best-fit SFH. The gray and light gray shaded regions show the 68% and 90% confidence interval, respectively. The blue vertical line shows the $\langle \mathrm{SFR} \rangle_{\mathrm{main}}$.

clouds and diffuse dust screen components. Adopting the prescription of Noll et al. (2009), the optical depth of the former follows

$$\hat{\tau}_{\lambda,1} = \hat{\tau}_1 (\lambda / 5500\ \text{Å})^{-1.0},$$

and the latter follows

$$\hat{\tau}_{\lambda,2} = \frac{\hat{\tau}_2}{4.05} (k'(\lambda) + D(\lambda)) \left(\frac{\lambda}{\lambda_V} \right)^n,$$

where $\hat{\tau}_2$ controls the normalization of the diffuse dust, n is the diffuse dust attenuation index, $k'(\lambda)$ is the Calzetti (2001) attenuation curve, and $D(\lambda)$ is a Lorentzian-like Drude profile describing the UV dust bump. The strength of the UV dust bump is tied to the best-fit diffuse dust attenuation index following the results of Kriek & Conroy (2013). A flat prior over $0 < \hat{\tau}_{\lambda,2} < 4$, a flat prior over $0 < \hat{\tau}_{\lambda,1} < 4$, and a flat prior over $-2.2 < n < 0.4$ are adopted. This flexible dust attenuation law can handle dust attenuation law variation where Kriek & Conroy (2013) reported that galaxies with lower specific SFR tend to have larger dust attenuation indices. Here, the AGN SED templates in Nenkova et al. (2008a, 2008b) are adopted. The contribution of an AGN is controlled with the AGN luminosity as a fraction of the galaxy bolometric luminosity (f_{AGN}) and optical depth of AGN torus dust (τ_{AGN}).

We show the SFH measured with the (i) model in Figure 5 in the main text. The corner plot of the parameters for (i) and (ii) models is shown in Figure B3. We show the SFH measured with (ii) to (iv) models in Figure B4. The corner plot of the parameters for (iii) and (iv) models is shown in Figure B5. For the purpose of illustration, the corner plots are shown for the modeling with the number of time bins $N = 7$, which gives parameters consistent with those evaluated with 14 time bins. We also test the Calzetti (2001) dust attenuation curve for the Dirichlet prior, but it does not change these parameters significantly. The AGN component in our target is negligible. Based on the above, the difference between the continuity SFH model and Prospector-α model mostly comes from the different SFH priors.

All (i) to (iv) models results in similar $\hat{\tau}_2$ and stellar mass. They are in agreement with the quiescence of the star formation in our target. In case of the continuity SFH prior, the modeling with free metallicity results in solar metallicity, while that for Prospector-α results in $\log Z/Z_{\odot} \sim -1$. As a result of the low luminosity, the SFH from iv) modeling quenched star formation earlier than those from other models. Since our observational data has no significant indices to confirm the metallicity robustly, we adopt the parameters measured adopting the continuity SFH prior and solar metallicity as conservative estimates.

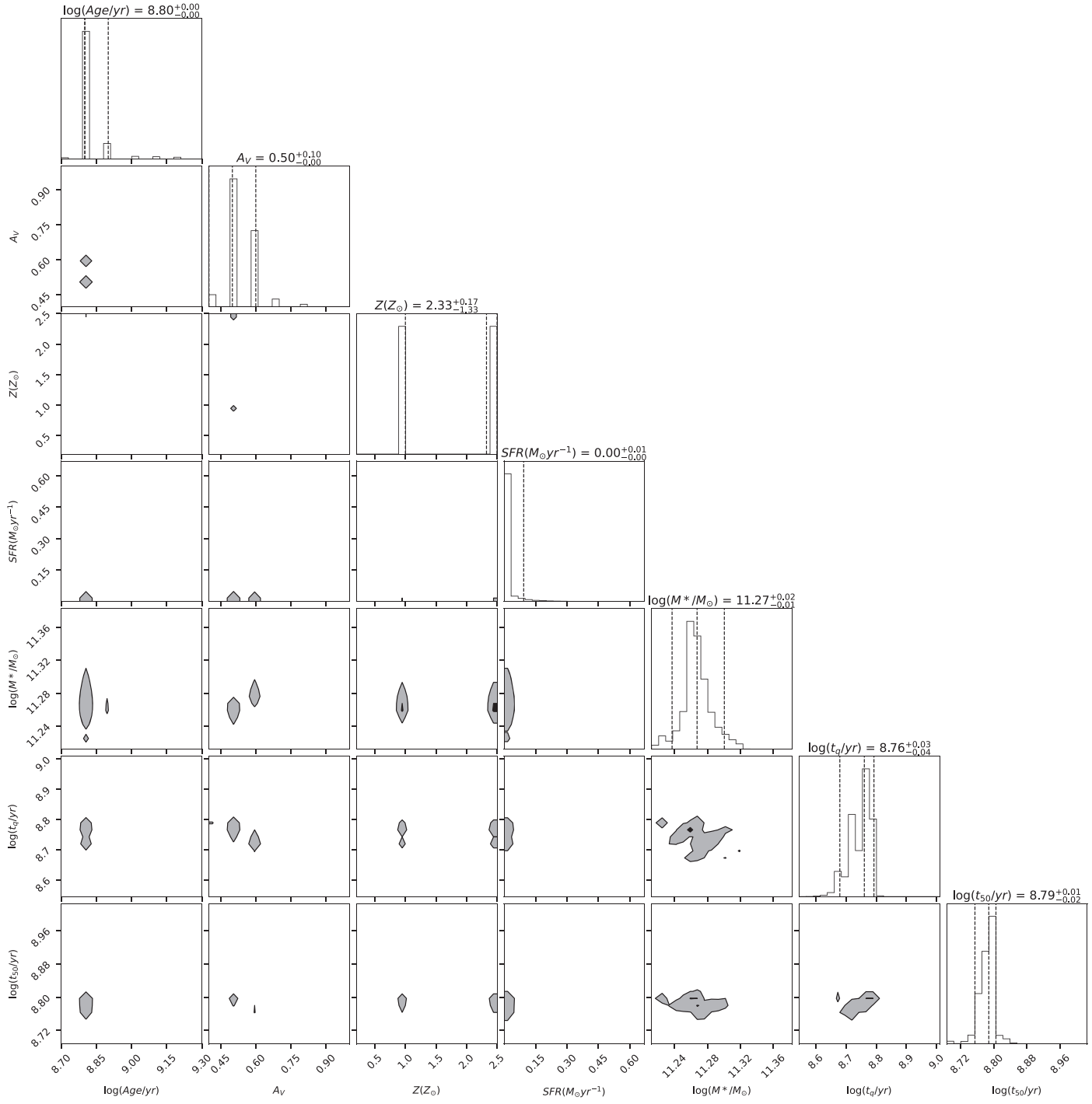

Figure B2. Corner plot for ADF22-QG1, showing the SED fitting covariance between the age, A_V, Z, SFR, t_{50}, and t_q. The black and gray shaded regions show the 68% and 95% confidence interval, respectively. The vertical dashed lines in the histograms show the 0.05, 0.5, and 0.95 quantiles of the probability distributions.

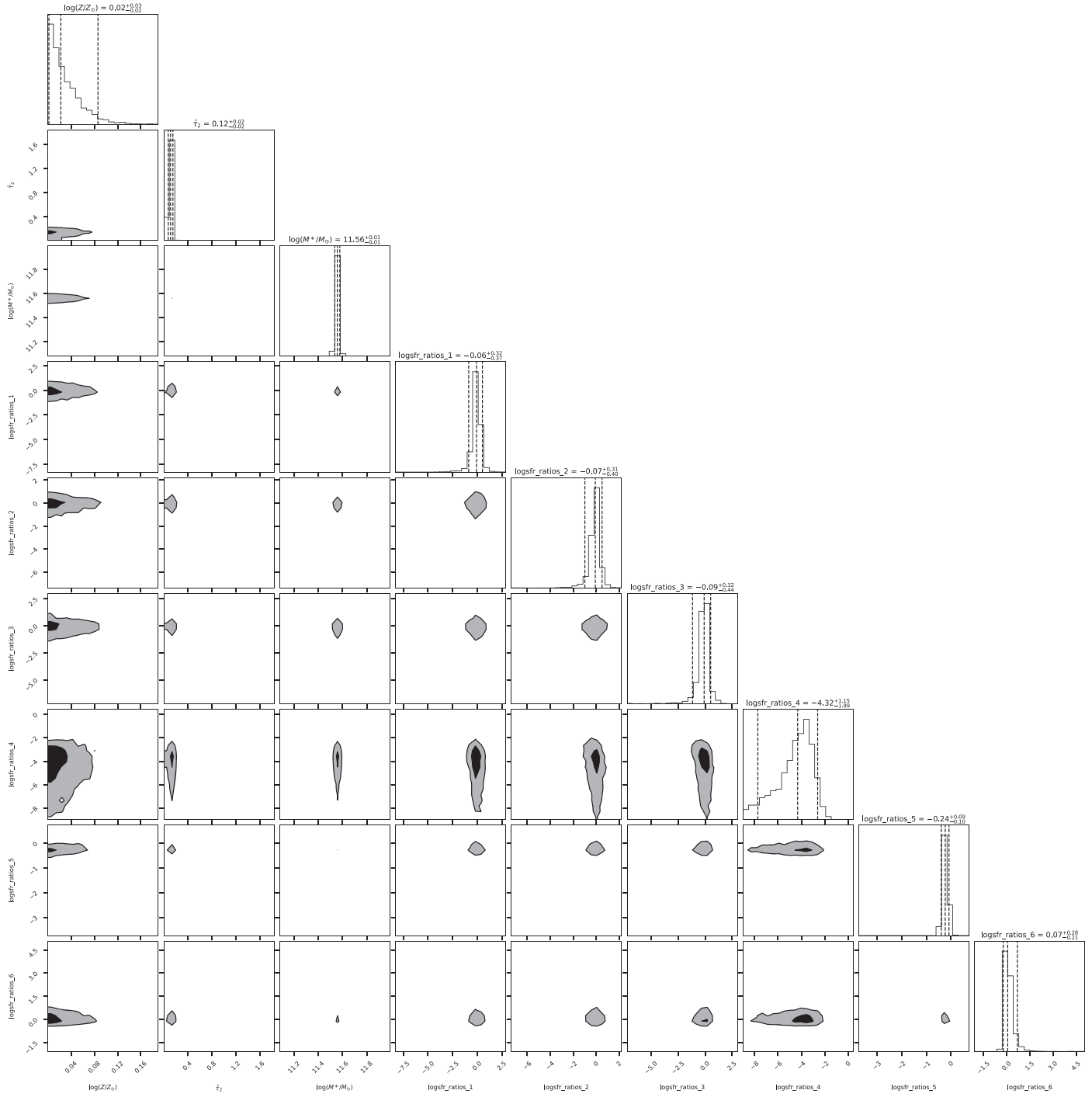

Figure B3. Similar to Figure B2, but computed with Prospector and adopting the continuity SFH prior. The parameters are $\log Z/Z_{\odot}$, $\hat{\tau}_2$, $\log (M_{\star}/M_{\odot})$ (logmass), and Δlog(SFR) between adjacent time bins (logsfr_ratio_n where $n = 1 - 7$).

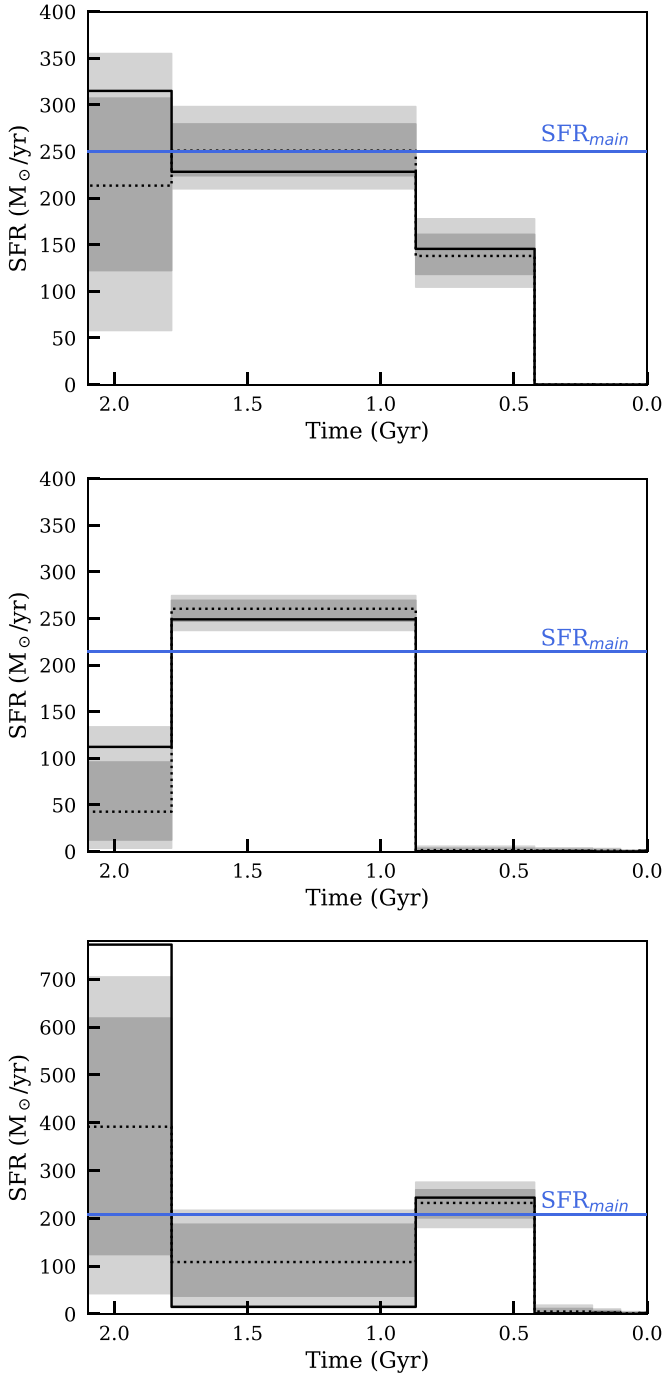

Figure B4. Similar to Figure 5, but measured with nonparametric SFH modelings. They are modeled with (ii) continuity SFH prior with free metallicity, (iii) Prospector-α SFH prior fixed with solar metallicity, and (iv) Prospector-α SFH prior with free metallicity, from top to bottom.

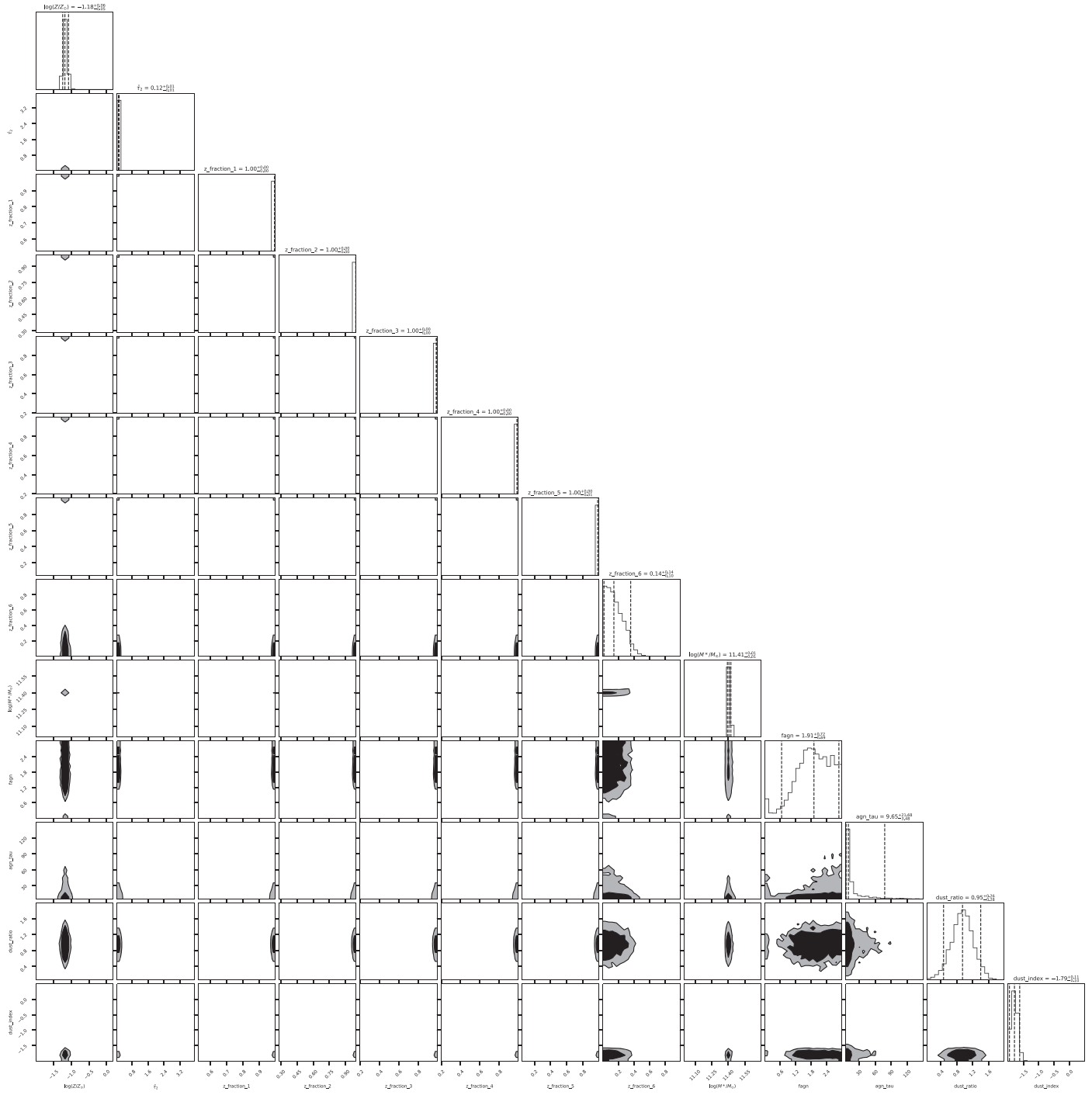

Figure B5. Similar to Figure B3, but adopting the Prospector-α SFH prior. The parameters are log $Z/Z_{\odot}$, $\hat{\tau}_2$, z_fraction, which is proportional to sSFR between adjacent time bins (z_fraction with $n = 1$–7), log $(M_{\star}/M_{\odot})$, AGN fraction (fagn), the optical depth for AGN (agn_tau), the ratio of $\hat{\tau}_1$ and $\hat{\tau}_2$ (dust_ratio), and n (dust_index).

ORCID iDs

Mariko Kubo https://orcid.org/0000-0002-7598-5292
Hideki Umehata https://orcid.org/0000-0003-1937-0573
Yuichi Matsuda https://orcid.org/0000-0003-1747-2891
Masaru Kajisawa https://orcid.org/0000-0002-1732-6387
Charles C. Steidel https://orcid.org/0000-0002-4834-7260
Ichi Tanaka https://orcid.org/0000-0002-4937-4738
Bunyo Hatsukade https://orcid.org/0000-0001-6469-8725
Yoichi Tamura https://orcid.org/0000-0003-4807-8117
Kouichiro Nakanishi https://orcid.org/0000-0002-6939-0372
Kotaro Kohno https://orcid.org/0000-0002-4052-2394
Kianhong Lee https://orcid.org/0000-0003-4814-0101

References

Akhshik, M., Whitaker, K. E., Leja, J., et al. 2021, ApJL, 907, L8
Andrews, B. H., & Thompson, T. A. 2011, ApJ, 727, 97
Barro, G., Faber, S. M., Koo, D. C., et al. 2017, ApJ, 840, 47
Barro, G., Faber, S. M., Pérez-González, P. G., et al. 2013, ApJ, 765, 104
Belli, S., Genzel, R., Förster Schreiber, N. M., et al. 2017, ApJL, 841, L6
Belli, S., Newman, A. B., & Ellis, R. S. 2015, ApJ, 799, 206

Belli, S., Newman, A. B., & Ellis, R. S. 2019, ApJ, 874, 17
Bezanson, R., van Dokkum, P. G., Tal, T., et al. 2009, ApJ, 697, 1290
Bruzual, G., & Charlot, S. 2003, MNRAS, 344, 1000
Burkert, A., Genzel, R., Bouché, N., et al. 2010, ApJ, 725, 2324
Calzetti, D. 2001, PASP, 113, 1449
Cappellari, M. 2017, MNRAS, 466, 798
Chabrier, G. 2003, PASP, 115, 763
Charlot, S., & Fall, S. M. 2000, ApJ, 539, 718
Conroy, C., Gunn, J. E., & White, M. 2009, ApJ, 699, 486
Daddi, E., Renzini, A., Pirzkal, N., et al. 2005, ApJ, 626, 680
Danielson, A. L. R., Swinbank, A. M., Smail, I., et al. 2017, ApJ, 840, 78
De Lucia, G., & Blaizot, J. 2007, MNRAS, 375, 2
Dekel, A., & Burkert, A. 2014, MNRAS, 438, 1870
Dekel, A., Sari, R., & Ceverino, D. 2009, ApJ, 703, 785
Doherty, M., Tanaka, M., De Breuck, C., et al. 2010, A&A, 509, A83
Evrard, A. E., Bialek, J., Busha, M., et al. 2008, ApJ, 672, 122
Fabricius, M., Walawender, J., Arimoto, N., et al. 2016, Proc. SPIE, 9908, 990828
Fan, L., Lapi, A., Bressan, A., et al. 2010, ApJ, 718, 1460
Fan, L., Lapi, A., De Zotti, G., et al. 2008, ApJL, 689, L101
Foreman-Mackey, D. 2016, JOSS, 1, 24
Forrest, B., Annunziatella, M., Wilson, G., et al. 2020, ApJL, 890, L1
Forrest, B., Marsan, Z. C., Annunziatella, M., et al. 2020, ApJ, 903, 47
Gobat, R., Strazzullo, V., Daddi, E., et al. 2013, ApJ, 776, 9
Gómez-Guijarro, C., Magdis, G. E., Valentino, F., et al. 2019, ApJ, 886, 88
Hayashino, T., Matsuda, Y., Tamura, H., et al. 2004, AJ, 128, 2073
Hill, R., Chapman, S., Scott, D., et al. 2020, MNRAS, 495, 3124
Ichikawa, T., Suzuki, R., Tokoku, C., et al. 2006, Proc. SPIE, 6269, 626916
Ito, K., Kashikawa, N., Toshikawa, J., et al. 2020, ApJ, 899, 5
Johnson, B., & Leja, J. 2017, Bd-J/Prospector: Initial Release, v1.0 Zenodo, doi:10.5281/zenodo.1116491
Kennicutt, R. C., & Evans, N. J. 2012, ARA&A, 50, 531
Kewley, L. J., Groves, B., Kauffmann, G., et al. 2006, MNRAS, 372, 961
Kodama, T., Tanaka, I., Kajisawa, M., et al. 2007, MNRAS, 377, 1717
Kriek, M., & Conroy, C. 2013, ApJL, 775, L16
Kriek, M., van Dokkum, P. G., Labbé, I., et al. 2009, ApJ, 700, 221
Kubo, M., Tanaka, M., Yabe, K., et al. 2018, ApJ, 867, 1
Kubo, M., Toshikawa, J., Kashikawa, N., et al. 2019, ApJ, 887, 214
Kubo, M., Uchimoto, Y. K., Yamada, T., et al. 2013, ApJ, 778, 170
Kubo, M., Yamada, T., Ichikawa, T., et al. 2015, ApJ, 799, 38
Kubo, M., Yamada, T., Ichikawa, T., et al. 2016, MNRAS, 455, 3333
Kubo, M., Yamada, T., Ichikawa, T., et al. 2017, MNRAS, 469, 2235
Labbé, I., Huang, J., Franx, M., et al. 2005, ApJL, 624, L81
Lamastra, A., Bianchi, S., Matt, G., et al. 2009, A&A, 504, 73
Lehmer, B. D., Alexander, D. M., Chapman, S. C., et al. 2009b, MNRAS, 400, 299
Lehmer, B. D., Alexander, D. M., Geach, J. E., et al. 2009a, ApJ, 691, 687
Leja, J., Carnall, A. C., Johnson, B. D., et al. 2019, ApJ, 876, 3
Leja, J., Johnson, B. D., Conroy, C., et al. 2017, ApJ, 837, 170
Lemaux, B. C., Lubin, L. M., Shapley, A., et al. 2010, ApJ, 716, 970
Long, A. S., Cooray, A., Ma, J., et al. 2020, ApJ, 898, 133
Lustig, P., Strazzullo, V., D'Eugenio, C., et al. 2021, MNRAS, 501, 2659
Matsuda, Y., Yamada, T., Hayashino, T., et al. 2005, ApJL, 634, L125
McLean, I. S., Steidel, C. C., Epps, H. W., et al. 2012, Proc. SPIE, 8446, 84460J
Mei, S., Scarlata, C., Pentericci, L., et al. 2015, ApJ, 804, 117
Miller, T. B., Chapman, S. C., Aravena, M., et al. 2018, Natur, 556, 469
Mizukoshi, S., Kohno, K., Egusa, F., et al. 2021, ApJ, 917, 94
Murray, N., Quataert, E., & Thompson, T. A. 2005, ApJ, 618, 569
Naab, T., Johansson, P. H., & Ostriker, J. P. 2009, ApJL, 699, L178
Navarro, J. F., Frenk, C. S., & White, S. D. M. 1997, ApJ, 490, 493
Nenkova, M., Sirocky, M. M., Ivezić, Ž, et al. 2008a, ApJ, 685, 147
Nenkova, M., Sirocky, M. M., Nikutta, R., et al. 2008b, ApJ, 685, 160
Noll, S., Burgarella, D., Giovannoli, E., et al. 2009, A&A, 507, 1793
Onodera, M., Carollo, C. M., Lilly, S., et al. 2016, ApJ, 822, 42
Osterbrock, D. E., & Ferland, G. J. 2006, in Astrophysics of Gaseous Nebulae and Active Galactic Nuclei, II, ed. D. E. Osterbrock & G. J. Ferland (Sausalito, CA: Univ. Science Books), 2006
Oteo, I., Ivison, R. J., Dunne, L., et al. 2016, ApJ, 827, 34
Oteo, I., Ivison, R. J., Dunne, L., et al. 2018, ApJ, 856, 72
Pavesi, R., Riechers, D. A., Sharon, C. E., et al. 2018, ApJ, 861, 43
Popping, G., Decarli, R., Man, A. W. S., et al. 2017, A&A, 602, A11
Rennehan, D., Babul, A., Hayward, C. C., et al. 2020, MNRAS, 493, 4607
Riechers, D. A., Bradford, C. M., Clements, D. L., et al. 2013, Natur, 496, 329
Rodríguez Montero, F., Davé, R., Wild, V., et al. 2019, MNRAS, 490, 2139
Rotermund, K. M., Chapman, S. C., Phadke, K. A., et al. 2021, MNRAS, 502, 1797
Santini, P., Merlin, E., Fontana, A., et al. 2019, MNRAS, 486, 560
Schlafly, E. F., & Finkbeiner, D. P. 2011, ApJ, 737, 103
Schreiber, C., Glazebrook, K., Nanayakkara, T., et al. 2018a, A&A, 618, A85
Schreiber, C., Glazebrook, K., Papovich, C., et al. 2021, A&A, 650, C2
Schreiber, C., Labbé, I., Glazebrook, K., et al. 2018b, A&A, 611, A22
Shi, K., Toshikawa, J., Cai, Z., et al. 2020, ApJ, 899, 79
Simpson, J. M., Smail, I., Swinbank, A. M., et al. 2015, ApJ, 807, 128
Speagle, J. S. 2020, MNRAS, 493, 3132
Spilker, J. S., Aravena, M., Phadke, K. A., et al. 2020, ApJ, 905, 86
Spilker, J. S., Bezanson, R., Marrone, D. P., et al. 2016, ApJ, 832, 19
Steidel, C. C., Adelberger, K. L., Dickinson, M., et al. 1998, ApJ, 492, 428
Steidel, C. C., Rudie, G. C., Strom, A. L., et al. 2014, ApJ, 795, 165
Strazzullo, V., Daddi, E., Gobat, R., et al. 2015, A&A, 576, L6
Strazzullo, V., Daddi, E., Gobat, R., et al. 2016, ApJL, 833, L20
Strazzullo, V., Gobat, R., Daddi, E., et al. 2013, ApJ, 772, 118
Suzuki, R., Tokoku, C., Ichikawa, T., et al. 2008, PASJ, 60, 1347
Tacchella, S., Conroy, C., Faber, S. M., et al. 2021, arXiv:2102.12494
Tamura, Y., Kohno, K., Nakanishi, K., et al. 2009, Natur, 459, 61
Tanaka, M., Valentino, F., Toft, S., et al. 2019, ApJL, 885, L34
Toft, S., Smolčić, V., Magnelli, B., et al. 2014, ApJ, 782, 68
Toshikawa, J., Uchiyama, H., Kashikawa, N., et al. 2018, PASJ, 70, S12
Umehata, H., Fumagalli, M., Smail, I., et al. 2019, Sci, 366, 97
Umehata, H., Hatsukade, B., Smail, I., et al. 2018, PASJ, 70, 65
Umehata, H., Tamura, Y., Kohno, K., et al. 2014, MNRAS, 440, 3462
Umehata, H., Tamura, Y., Kohno, K., et al. 2015, ApJL, 815, L8
Umehata, H., Tamura, Y., Kohno, K., et al. 2017, ApJ, 835, 98
Valentino, F., Tanaka, M., Davidzon, I., et al. 2020, ApJ, 889, 93
van der Wel, A., Franx, M., van Dokkum, P. G., et al. 2014, ApJ, 788, 28
van Dokkum, P. G., Bezanson, R., van der Wel, A., et al. 2014, ApJ, 791, 45
van Dokkum, P. G., Franx, M., Kriek, M., et al. 2008, ApJL, 677, L5
Walawender, J., Wung, M., Fabricius, M., et al. 2016, Proc. SPIE, 9908, 99082G
Wellons, S., Torrey, P., Ma, C.-P., et al. 2015, MNRAS, 449, 361
Wellons, S., Torrey, P., Ma, C.-P., et al. 2016, MNRAS, 456, 1030
Whitaker, K. E., van Dokkum, P. G., Brammer, G., et al. 2013, ApJL, 770, L39
Williams, C. C., Giavalisco, M., Cassata, P., et al. 2014, ApJ, 780, 1
Yamada, T., Nakamura, Y., Matsuda, Y., et al. 2012, AJ, 143, 79
Yan, R., Newman, J. A., Faber, S. M., et al. 2006, ApJ, 648, 281
Zirm, A. W., Stanford, S. A., Postman, M., et al. 2008, ApJ, 680, 224
Zolotov, A., Dekel, A., Mandelker, N., et al. 2015, MNRAS, 450, 2327